



# Synthesis of Compact and Porous SiO<sub>2</sub> Nanoparticles and Their Effect on Thermal Conductivity Enhancement of Water-Based Nanofluids

U. O. García-Vidal<sup>1</sup> · J. L. Jiménez-Pérez<sup>1</sup> · G. López-Gamboa<sup>2</sup> ·  
R. Gutiérrez-Fuentes<sup>3</sup> · J. F. Sánchez-Ramírez<sup>4</sup> · Z. N. Correa-Pacheco<sup>5</sup> ·  
I. C. Romero-Ibarra<sup>1</sup> · A. Cruz-Orea<sup>6</sup>

Received: 30 September 2022 / Accepted: 18 October 2022 / Published online: 1 November 2022  
© The Author(s), under exclusive licence to Springer Science+Business Media, LLC, part of Springer Nature 2022

## Abstract

In this work, compact and porous SiO<sub>2</sub> nanoparticles (NPs) were synthesized using the Stöber and the modified Stöber methods. Water-based nanofluids were characterized by dynamic light scattering, scanning electron microscopy, transmission electron microscopy, energy-dispersive spectroscopy, Fourier transform infrared spectroscopy, and X-ray diffraction, and the porosity of the compact and porous SiO<sub>2</sub> samples was measured by N<sub>2</sub> adsorption–desorption isotherms. Thermal wave resonator cavity and inverse photopyroelectric configuration novel techniques were used for the first time to obtain the porous nanoparticles thermal diffusivity ( $D$ ) and effusivity ( $e$ ), respectively. Thermal conductivity ( $k$ ) was obtained from the relationship between them  $k = e\sqrt{D}$ . An increase in the thermal conductivity of the porous SiO<sub>2</sub> NPs was obtained compared to the thermal conductivity of the compact NPs fluids with an enrichment of 14.7%. Our results are supported by a theoretical model with a thermodynamic approach adapted for the thermal conductivity of porous SiO<sub>2</sub> governed by the parameters of the porosity and nanoparticle size.

**Keywords** Nanofluids · SiO<sub>2</sub> nanoparticles · Thermal conductivity

## 1 Introduction

Mesoporous silica materials have received great attention in the industry due to their high chemical and thermal stability and their non-toxic nature [1, 2]. Therefore, it can be used in medicine, biology [2, 3], and inorganic optoelectronic devices [4, 5]. Because silica is a chemically and thermally stable material, it can be added to metal

---

✉ J. L. Jiménez-Pérez  
jimenezp1957@gmail.com

Extended author information available on the last page of the article

nanoparticles for heat exchange applications [1]. Nanocomposites offer unique properties to control thermal transport by manipulating various structural aspects of the material. Measurement of thermal properties of porous nanomaterials is often difficult to determine, moreover, in the optical field due to the non-contact nature [6]. Among the advantages of these types of nanostructures, their structural properties, such as large surface area and pore volume, adjustable pore size, colloidal stability, and the possibility of functionalizing internal pore systems or the external surface of the particle are noteworthy. These features make it a promising material for biomedical applications such as bioimaging for diagnosis [7–14] or drug delivery for medical applications [7–15]. In recent decades, there has been great interest for photothermal techniques such as thermal lens [16–18], photoacoustic [19], and thermal wave resonator cavity (TWRC) [20, 21]. In the present research, the conventional TWRC was used to measure the thermal diffusivity of nanofluids. This technique is frequently used in different applications for liquids and gases. Although other photothermal techniques have been used for thermal characterization of liquids, such as thermal lens spectroscopy (TLS), photothermal deflection, photoacoustic spectroscopy, and photothermal radiometry [16–22], the TWRC technique is of special interest because it allows measurement of nanofluids' thermal diffusivity in small volume detection cells. To have a complete thermal characterization of the thermal conductivity, the thermal effusivity of the studied nanofluids was obtained using IPPE configuration. Complementary characterization, to determine particle size and chemical composition, was performed by dynamic light scattering (DLS), scanning electron microscopy (SEM), transmission electron microscopy (TEM), energy-dispersive spectroscopy (EDS), Fourier transform infrared spectroscopy (FTIR), and X-ray diffraction (XRD) techniques, and porosity was determined by  $N_2$  adsorption–desorption isotherms.

## 2 Materials and Methods

### 2.1 Materials

The Stöber and the modified Stöber method were used for the synthesis of compact and porous  $SiO_2$  NPs, respectively [23, 24]. Reagents used for  $SiO_2$  nanostructures were tetraethyl orthosilicate (TEOS, 99 %), ammonium hydroxide ( $NH_4OH$  30 % ammonia  $NH_3$ ), methanol ( $CH_3OH$  99 %), ethanol ( $C_2H_5OH$  99 %), and sodium hydroxide ( $NaOH$  99 %). All were purchased from Sigma-Aldrich. Deionized water was used for the nanofluids.

### 2.2 Methods

#### 2.2.1 Synthesis of Compact and Porous $SiO_2$ NPs

Briefly, 60 mL of an ethanol solution containing 25 mL of distilled water, 1 mL of TEOS, and 4.2 mL of ammonia hydroxide was prepared. It was stirred at 300 rpm

for 3.5 h at room temperature to carry out the TEOS hydrolysis and condensation process. The resulting colloidal suspension was centrifuged at 4000 rpm for 15 min. The particles were recovered and washed with a methanol/water 1:1 volume ratio solution, repeating the process at least 5 times. Finally, they were left to dry in a muffle at 70 °C [18].

The synthesis of porous SiO<sub>2</sub> NPs was as follows: 0.2 g of CTAB (cetyl trimethyl ammonium bromide) surfactant and 1 mL of TEOS silica precursor (tetraethyl orthosilicate) were weighed and a basic 2 mol of NaOH solution was prepared. On a heating plate, the CTAB surfactant was placed in a round flask with 100 mL of distilled water. It was stirred at 200 rpm, and the temperature was raised to 30 °C, at which point the solution turned on transparent. Then, 1 mL of NaOH solution was added to have a basic solution with a pH of 12. The temperature was raised to 80 °C and maintained at 200 rpm. At 80°C, stirring was increased to 500 rpm, and the TEOS silica precursor was added at a speed of 1 mL·min<sup>-1</sup> through a syringe infusion pump using a temperature and pH meters built in the laboratory with a 3D printer, as shown in Fig. 1a, b. The transparent solution began to turn on cloudy white, at which point the nucleation and growth of the silica particles are known to start [25].

The synthesis was carried out for 2 h. Then, the reaction was neutralized with sulfuric acid to a pH of 7 to stop the nanoparticles' growth. The obtained solution was centrifuged at 4000 rpm for 10 min, and the white precipitate was placed in a flask and stirred at 200 rpm for 10 min with distilled water. This procedure was followed at least 3 times to wash the NPs. When the particles were washed, to remove the surfactant or organic template, they were subjected to a thermal treatment in a muffle. The white precipitate was placed in a high-temperature crucible ramp and heating at 10 °C·min<sup>-1</sup> until 550°C for 4 h and finally, allowed to cool to room temperature. A white powder was obtained due to the porous NPs formation, as shown in Fig. 2. After that, it was pulverized in a mortar [24, 26].

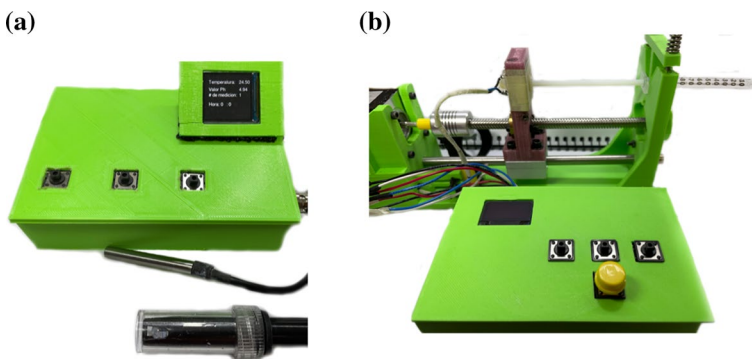


**Fig. 1** (a) Equipment for temperature and pH measurement and (b) syringe infusion pump



**Fig. 2** Synthesis of compact and porous SiO<sub>2</sub> NPs

### 2.2.2 DLS, SEM, TEM, and EDS Measurements

To determine the particle size of the NPs in the nanofluid, DLS was used (Litesizer 500, Anton Paar). SEM was performed using a JEOL model IT 300 scanning electron microscope with an acceleration voltage of 20 kV. The sample was placed on the carbon tape of a holder. TEM was performed on a JEOL model JEM-1010 transmission electron microscope, using an acceleration voltage of 60 kV. The sample was placed on a copper grid. EDS was performed using a SEM/EDS microscope JEOL JSM IT300.

### 2.2.3 FTIR Characterization

SiO<sub>2</sub> synthesized in both reactions was characterized by Fourier transform infrared spectroscopy (FTIR) using a Bruker FTIR ALPHA II spectrometer with an attenuated total reflection (ATR) accessory. Spectra were normalized for comparison purposes.

### 2.2.4 XRD Determination

The small-angle X-ray diffraction (XRD) patterns of the samples were collected with a diffractometer (Rigaku) equipped with a rotating anode and using Cu K $\alpha$  radiation ( $\lambda=0.1542$  nm), voltage and current of 40 kV and 100 mA, respectively. XRD data were recorded for reflection angle in the range of  $1.5^\circ \leq 2\theta \leq 8.96^\circ$  with a step size of 0.02.

### 2.2.5 N<sub>2</sub> Adsorption–Desorption Isotherms

The specific surface area and pore size distribution were estimated by Brunauer–Emmett–Teller (BET) equation and Barrett–Joyner–Halenda (BJH)

method, respectively. Surface area analyses were performed on a Quantachrome autosorb iQ equipment. The N<sub>2</sub> adsorption–desorption isotherms were determined at 77 K by volumetric adsorption. Before the N<sub>2</sub> adsorption process, all the samples were outgassed at 80 °C for 4 h.

### 2.2.6 Thermal Properties Measurement

**2.2.6.1 Thermal Diffusivity Measurements** The TWRC experimental setup with pyroelectric sensor was used to obtain the sample thermal diffusivity. This thermal parameter was obtained by making a scanning of the nanofluid as shown in Fig. 3a. A modulated laser beam, with modulation frequency  $f$  and 40 mW power, is guided into a cylindrical cavity with one end covered by an Al foil. The radiation is absorbed by the Al foil and is transmitted to the sample. The heat generated in the sample diffuses through the liquid medium to reach the pyroelectric sensor, which senses the diffused heat and generates an electrical signal, which is recorded and processed as shown in Fig. 3b [21].

The cylindrical cavity, 2 cm length, with a diameter of 10 mm and 50 μm thick (stainless-steel film) contains the liquid sample to be analyzed, covering the PZT sensor of 50 microns. The diode laser beam, 660 nm wavelength, is modulated at a fixed frequency of  $f=0.25$  Hz. The absorption of the modulated light beam induces a modulated temperature variation in the liquid sample. The temperature oscillations at  $x=-l-L$  were measured with the PPE sensor as a function of the thickness of liquid sample. The signal was sent to a preamplifier and then a second lock-in amplifier (model SR810 DSP), where its amplitude and phase are measured as a function of  $L$ .

By considering the TWRC theoretical model, for thermally thick samples,  $qLs \gg 1$ , where  $q = \left(\frac{2\pi fi}{D}\right)^{1/2}$  with  $\alpha$  and  $Ls$  the sample thermal diffusivity and

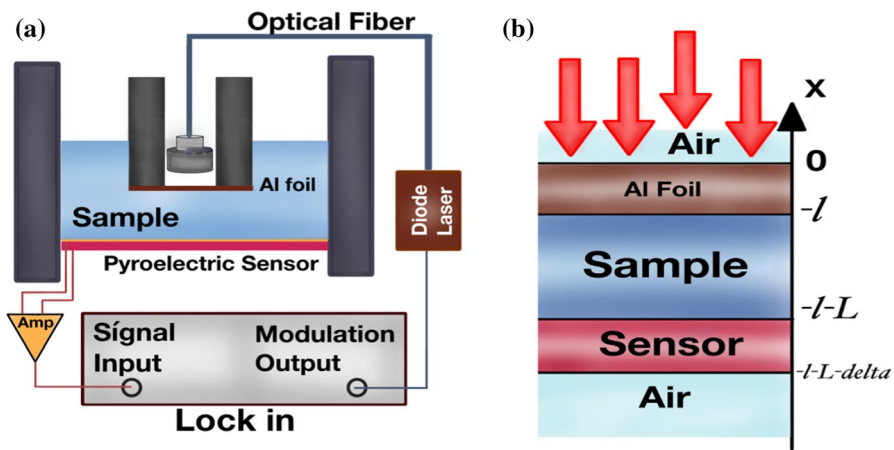


Fig. 3 TWRC configuration: (a) Experimental setup (b) Multi-layered theoretical model

cavity length, respectively. Then the sensor output voltage is a complex expression that can be written as follows [27]:

$$V(Ls) = V_0 e^{-qLs}, \tag{1}$$

where  $V_0$  is the initial voltage.

Equation 1 shows that it is possible to perform simple TWRC measurements to obtain the thermal diffusivity of liquids by monitoring the PPE pyroelectric sensor signal as a function of cavity length and fitting the data into the linear equation on a logarithmic scale, and the thermal diffusivity can be obtained from the slope fit parameter  $q$  [27–29].

**2.2.6.2 Thermal Effusivity Measurements** To obtain a complete thermal characterization, it is necessary to know the sample thermal effusivity as well as thermal conductivity. In this sense, the PPE technique was used in the inverse geometry (IPPE) configuration as shown in Fig. 4 to obtain the thermal effusivity of the samples [28].

The experimental setup (Fig. 4a) consisted of a commercial 50- $\mu\text{m}$ -thick PZT sensor (PUI Audio, model AB2022A, 80,000 pF). A semiconductor diode laser (model IFLEX-2000) is controlled by the TTL output of the lock-in amplifier (Stanford Research Systems, model SR830). The PPE signal feeds a preamplifier (Stanford Research Systems, SR540) and is sent to the lock-in amplifier. The pyroelectric signal was taken in a range frequency from 0.6 Hz to 10 Hz in steps of 0.5 Hz and the reference sample (water).

In IPPE configuration, the sample is placed on top of a pyroelectric transducer where, on the opposite side, it is uniformly irradiated with modulated light with frequency  $f$ . The transducer absorbs light and is optically opaque where the resulting signal will be independent of the optical properties of sample. The theoretical model

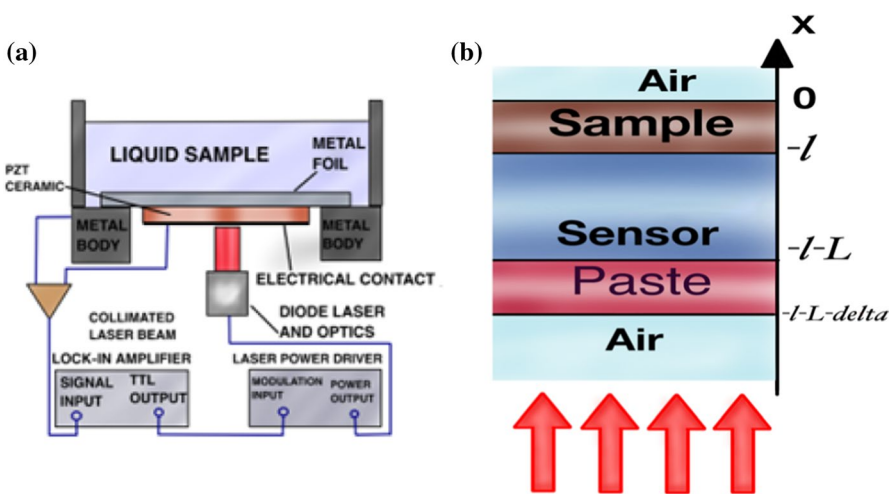


Fig. 4 IPPE configuration: (a) Experimental setup (b) Multi-layered theoretical model

of the distribution of temperature oscillations for this configuration was deduced by Caerels et al. [28] using the 3-layer model see Fig. 4b.

In the case of a thermally thick sample, the distribution of complex temperature  $\theta(\omega)$  can be approximated by [30]:

$$\theta(\omega) = \frac{[(1 - e^{\sigma_p l_p})(1 + b) + (e^{-\sigma_p l_p} - 1)(1 - b)]}{[(g - 1)(1 - b)e^{-\sigma_p l_p} + (1 + g)(1 + b)e^{\sigma_p l_p}]}, \quad (2)$$

where  $\theta(\omega)$  is the output signal of the pyroelectric detector,  $\omega = 2\pi f$ ,  $\sigma_p = \frac{1+i}{\mu_p}$ ,  $\mu_p = \sqrt{\frac{\alpha_p}{\pi f}}$ ,  $\alpha_p$ ,  $l_p$  are the pyroelectric thermal diffusivity and its thickness, respectively,  $b = \frac{e_s}{e_p}$  y  $g = \frac{e_g}{e_p}$ , with  $e_s$ ,  $e_g$ , and  $e_p$  are the sample, gas (air), and pyroelectric thermal effusivity, respectively. Taking the PPE signal as a function of frequency, it is possible to obtain the sample thermal effusivity from the best fit of Eq. 2 to the experimental data, with  $b$  as the adjustment parameter. To avoid the dependence of the pyroelectric signal on  $f$ , the obtained signal was normalized with the PPE signal from empty cell (air) [29].

To determine the thermal effusivity as a function of frequency, the IPPE configuration was used. The measurements of the compact and porous SiO<sub>2</sub> NPs were carried out in water base, and concentration was 1 mg·mL<sup>-1</sup>. Before measurement, the samples were placed in an ultrasonic bath for 10 min to homogenize. 1 mL of the solution was placed inside the cavity of the IPPE configuration with a micropipette to ensure the volume to be measured. The calibration of thermal effusivity was done in water, and 6 measurements were performed for each sample.

### 3 Results and Discussion

The conventional method for the compact SiO<sub>2</sub> in comparison with the modified method to obtain SiO<sub>2</sub> of porous structure reduces the reaction time, improving the synthesis. In addition, the synthesis method developed in this work decreased the reaction time compared to the previously reported. The results for the nanoparticles characterization are shown.

#### 3.1 DLS, SEM, TEM, and EDS Measurements

Through DLS and SEM techniques, the diameter of the compact SiO<sub>2</sub> particles with a size of  $216 \pm 13$  nm was determined as shown in Fig. 5.

DLS and SEM techniques differ in sample preparation. For DLS, prior to measurement, the sample is sonicated, and on testing, nanoparticles are suspended in the solution showing a size distribution. In the case of SEM, a drop of the sample is placed on the carbon tape and during drying, there is a volumetric contraction of the drop, hence, agglomerates can form. If the nanoparticles in Fig. 5 are observed in detail in the SEM micrograph, the size corresponds in the scale to approximately 216 nm, in agreement with the value of the Gaussian peak for the DLS.

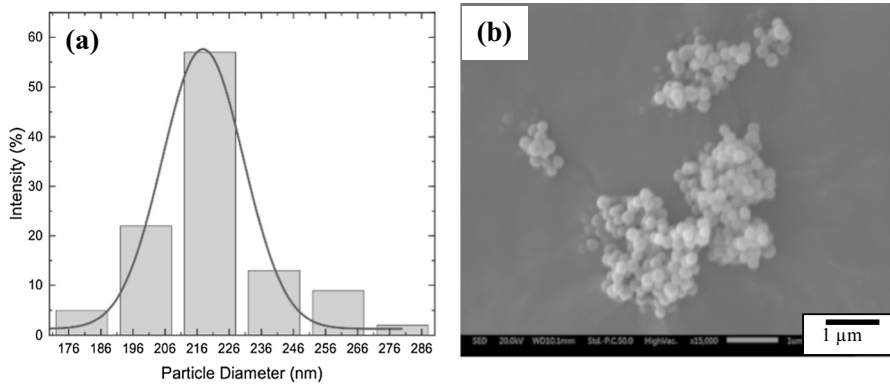


**Fig. 5** Estimation of the diameter of the compact SiO<sub>2</sub> NPs by (a) DLS technique (b) SEM

Also, for the measurement of the particle size distribution for the porous SiO<sub>2</sub> particles, DLS and SEM techniques were used. The obtained value was  $207 \pm 44$  nm. Both techniques showed close values. Moreover, a pore size of 2.5 nm was observed by TEM as shown in Fig. 6. Both techniques are different; in SEM, the electron beam scans the surface of the sample, and for TEM, electrons are transmitted through the sample.

On the other hand, the chemical composition of the SiO<sub>2</sub> NPs was determined using EDS analysis. The elements correspond to those found in the literature for compact and porous SiO<sub>2</sub> NPs. The composition of the samples was mainly silicon (Si) and oxygen (O) with 67.89 wt% (78.72% mol) and Si 32.11wt% (21% mol), which shows that the sample is 100% SiO<sub>2</sub>, as seen in Fig. 7.

### 3.2 FTIR Characterization

Characterization by infrared spectroscopy of compact (interdotted line) and porous (dotted line) of SiO<sub>2</sub> nanoparticles is shown in Fig. 8, in which the absorption bands associated with the characteristic stretching, bending, and wagging vibrations of the SiO<sub>2</sub> group are shown. The main absorption peaks are located at  $3400 \text{ cm}^{-1}$ , 2350

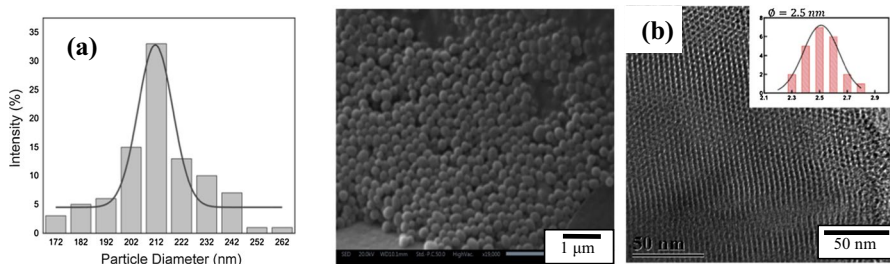


**Fig. 6** Estimation of the diameter of the porous SiO<sub>2</sub> NPs by (a) DLS and SEM (b) TEM



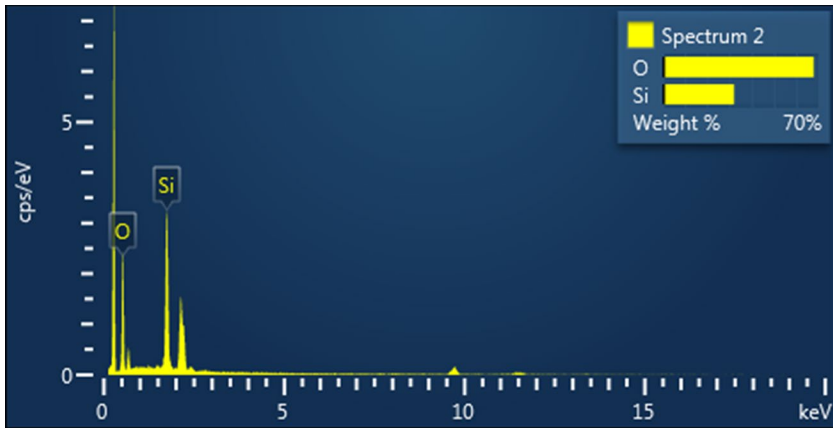


Fig. 7 Typical spectrum of the SiO<sub>2</sub> NPs with the EDS technique

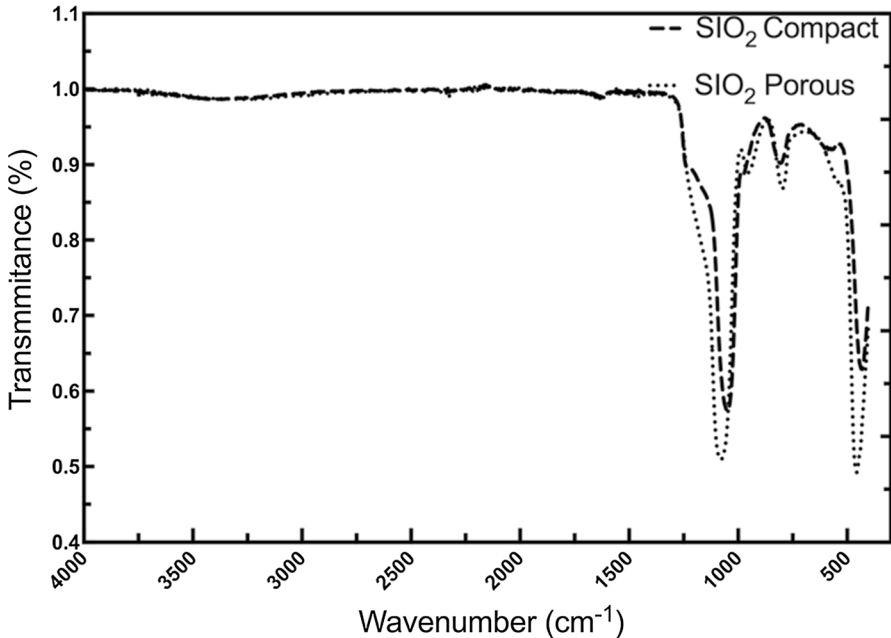


Fig. 8 Characterization by FTIR of compact and porous SiO<sub>2</sub> NPs

cm<sup>-1</sup>, 1630 cm<sup>-1</sup>, 1200 cm<sup>-1</sup>, 1100 cm<sup>-1</sup>, 960 cm<sup>-1</sup>, 800 cm<sup>-1</sup>, and 470 cm<sup>-1</sup>. For the compact SiO<sub>2</sub>, it is observed that the typical vibrations for SiO<sub>2</sub> are located at 1100 cm<sup>-1</sup>, 800 cm<sup>-1</sup>, and 470 cm<sup>-1</sup> corresponding to the stretch bonds of silicon with oxygen [31, 32].

Peaks at 460, 795, and 1075 cm<sup>-1</sup> are related to the rocking bending, symmetric, and asymmetric vibrations of Si–O–Si. The strongest peak attributed to Si–O bond

stretching is located at  $1100\text{ cm}^{-1}$ , while the  $800$  and  $470\text{ cm}^{-1}$  peaks are related to O–Si–O and Si–O–Si bending of these groups [33]. The  $3400\text{ cm}^{-1}$  vibration is due to the stretching of the OH band in the Si–OH and water structures [34]. The peak at  $2350\text{ cm}^{-1}$  is attributed to the carbon dioxide group, as well as the peak at  $1630\text{ cm}^{-1}$ . Also, this peak  $1638\text{ cm}^{-1}$  is attributed to the adsorbed water molecules. It found a shoulder at  $1200\text{ cm}^{-1}$  close to the strong  $1100\text{ cm}^{-1}$  peak due to Si–O–Si stretching. The  $960\text{ cm}^{-1}$  band is associated to the high surface area of silicon and directly related to the surface silanol groups. Silanol is a functional group in silicon chemistry with the Si–O–H connectivity and is assigned to the Si–OH stretching vibration [33, 34].

### 3.3 XRD Determination

Figure 9 shows the XRD pattern of the porous SiO<sub>2</sub> sample, and the sharp, low-angle (100) reflection peak demonstrates the characteristic of a typical mesoporous structure. The relatively weak peaks indexed to the (110), (200), and (210) reflections of the hexagonal-2d (p6 mm) mesostructure confirm the highly ordered mesostructure of the silica host [35]. Moreover, the XRD pattern revealed that the intensities of the four peaks are related to the ordered hexagonal structure observed for porous SiO<sub>2</sub> (calcined at 550°C) [36, 37].

In the inset in Fig. 9, the formation of compact pure SiO<sub>2</sub> NPs was also confirmed by XRD analysis. The broad X-ray diffraction pattern of the silica indicates a typical

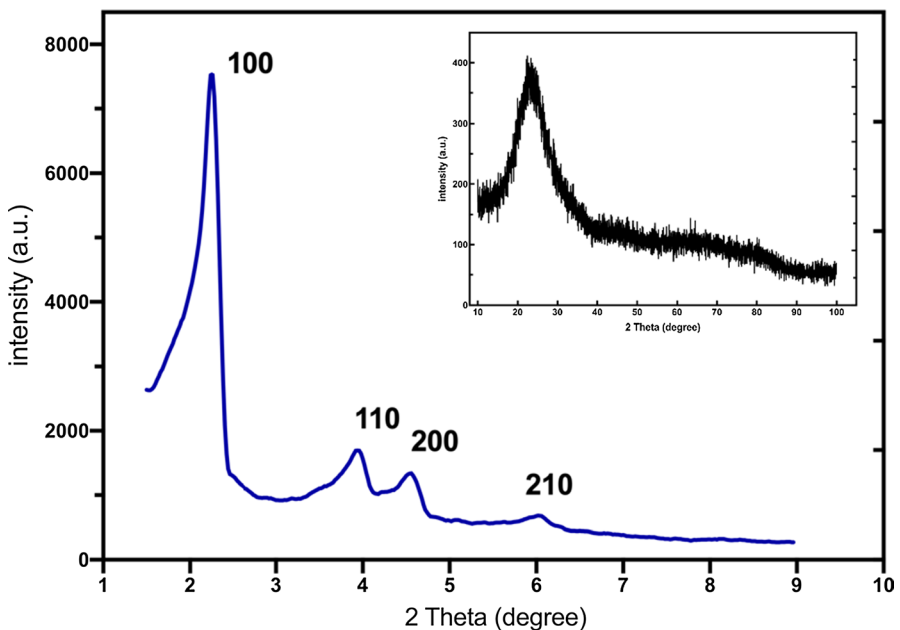
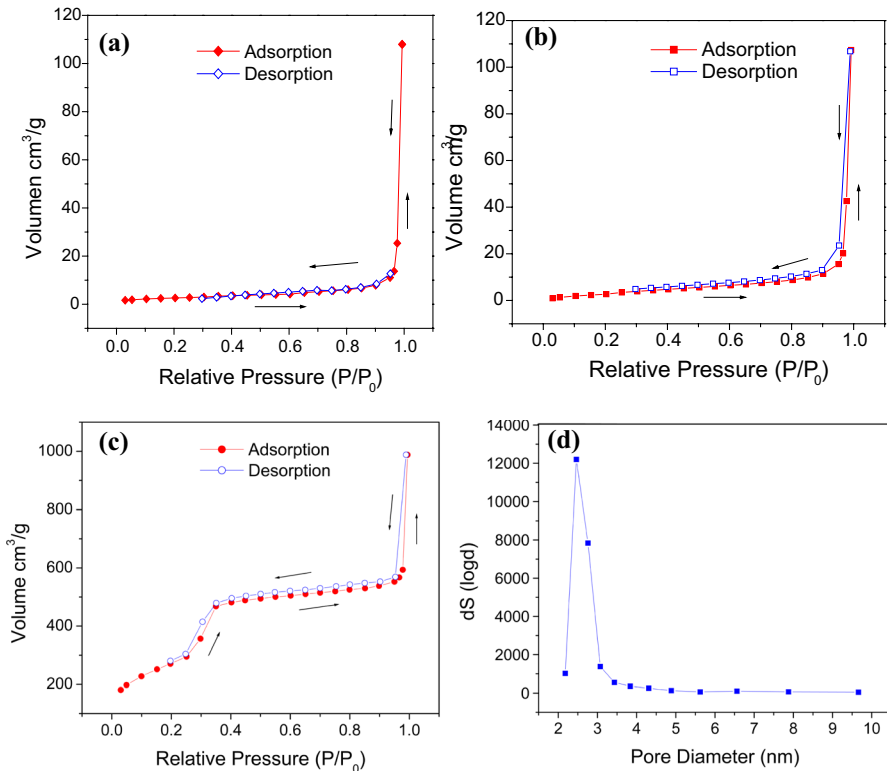


Fig. 9 Characterization by XRD of porous SiO<sub>2</sub> NPs

form of amorphous solids and further confirmed the absence of any ordered crystalline structure. A broad peak ( $2\theta=22^\circ$ , (101)) confirmed the amorphous nature of the silica [38, 39].

### 3.4 N<sub>2</sub> Adsorption–Desorption Isotherms

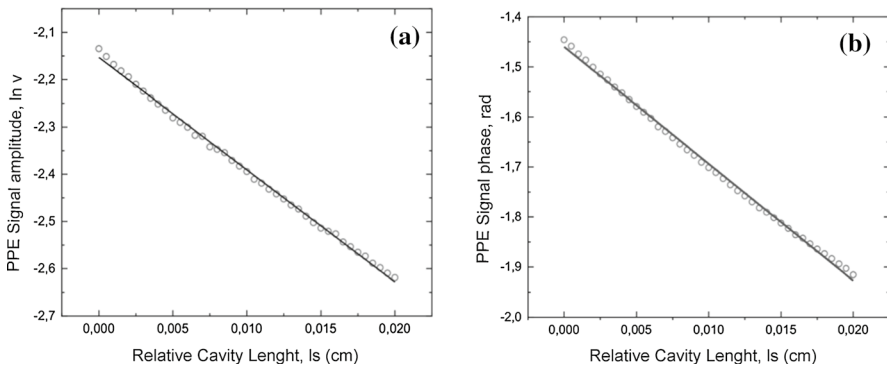
Figure 10 shows the N<sub>2</sub> adsorption–desorption isotherms for both compact and porous SiO<sub>2</sub> samples. The curve of Figs. 10a, b corresponds to a compact SiO<sub>2</sub> with type II-b isotherm according to the IUPAC classification, with very narrow b points at around 0.05 of  $P/P_0$ . This behavior of isotherm is typical of dense aggregate of particles and non-porous surfaces, which is in good agreement to the SEM analysis. Moreover, the surface area of the sample was estimated to be  $8.4 \text{ m}^2\cdot\text{g}^{-1}$  (Fig. 10a) and  $13.2 \text{ m}^2\cdot\text{g}^{-1}$  (Fig. 10b) using the Brunauer–Emmett–Teller ( $S_{\text{BET}}$ ) model [40]. The hysteresis depicted on the SiO<sub>2</sub> sample with  $13.2 \text{ m}^2\cdot\text{g}^{-1}$  (Fig. 10b) must be neglected, due to the very low-gas volume adsorbed which is assigned to materials consisting of agglomerates of fine particles forming interparticle mesopores [41]. Additionally, Fig. 10c shows the N<sub>2</sub> adsorption–desorption isotherm of porous



**Fig. 10** N<sub>2</sub> adsorption–desorption isotherms of SiO<sub>2</sub> (a) and (b) compact, (c) porous samples and (d) BJH model for SiO<sub>2</sub> porous sample

**Table 1** Surface area determination for the compact and porous samples

Sample	Surface area $S_{\text{BET}}$ ( $\text{m}^2 \cdot \text{g}^{-1}$ )	Average pore size (nm)	Pore volume ( $\text{cm}^3 \cdot \text{g}^{-1}$ )
Compact $\text{SiO}_2$ (Fig. 10a)	8.4	–	–
Compact $\text{SiO}_2$ (Fig. 10b)	13.3	–	–
Porous $\text{SiO}_2$ (Fig. 10c)	1121.5	2.46	1.55

**Fig. 11** Typical PPE signal  $\ln$  (a) amplitude and (b) phase as a function of the length of distilled water sample for system calibration

$\text{SiO}_2$  sample that was identified as isotherm type IV, which is a typical feature of mesoporous materials, according to the IUPAC's conventional classification. The BET model enables to estimate high surface area of  $1121.5 \text{ m}^2 \cdot \text{g}^{-1}$ . Figure 10d discloses the pore size distribution of this sample. It was estimated from the isotherm using the BJH model that shows the average pore diameter of 2.46 nm and the total pore volume is  $1.55 \text{ cm}^3 \cdot \text{g}^{-1}$ . The values of  $S_{\text{BET}}$ , pore size determination of porous material, total volume, and pore diameter are listed in Table 1.

As indicated by Table 1, the porous  $\text{SiO}_2$  sample exhibits a surface area of  $1121.4 \text{ m}^2 \cdot \text{g}^{-1}$ , which is very large in comparison with the compact area of the compact NPs. These results evidence that the microstructural characterization previously analyzed by SEM is in concordance with the synthesis method and pore diameter.

### 3.5 Thermal Diffusivity Obtained by TWRC Technique

The characteristic PPE signal of the TWRC, as a function of sample length in the cavity, for distilled water sample is shown in Fig. 11. The amplitude and phase signals can be seen as a function of the cavity length. The solid line in Fig. 11a, b shows the best fit of Eq. 1 to the experimental data for  $\ln$  of amplitude and phase, respectively. From these fits, the water thermal diffusivities were  $1.40 \pm 0.02 \times 10^{-3} \text{ cm}^2 \cdot \text{s}^{-1}$  and  $1.44 \pm 0.02 \times 10^{-3} \text{ cm}^2 \cdot \text{s}^{-1}$  for fixed 0.25 Hz frequency. These values

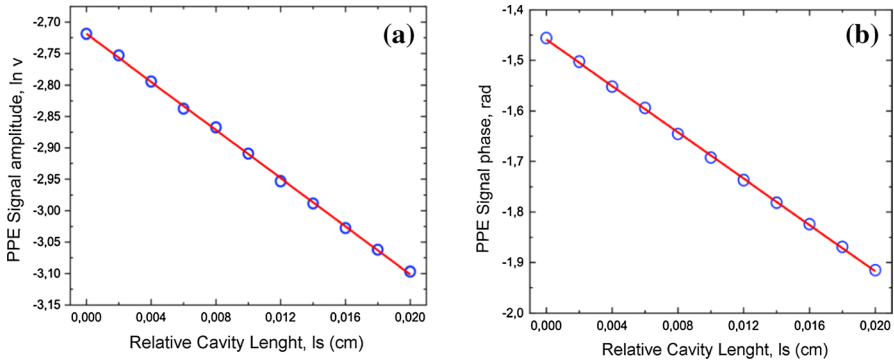


**Fig. 12** Pyroelectric signal of ln (a) amplitude and (b) phase of compact  $\text{SiO}_2$  nanoliquids of  $216 \pm 13$  nm in water base as a function of the sample length in the cavity

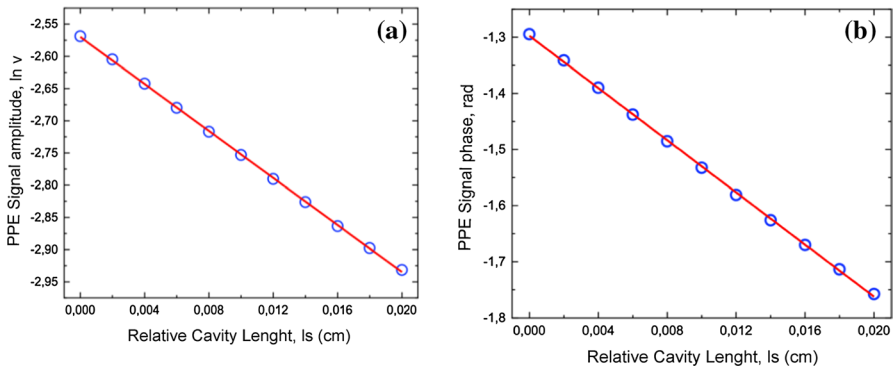


**Fig. 13** Pyroelectric signal of the ln (a) amplitude and (b) phase of the porous  $\text{SiO}_2$  nanoliquids of  $207 \pm 44$  nm in water base as a function of the sample length in the cavity

agree with the experimental and theoretical values reported in the literature [27, 30, 42].

The thermal diffusivity determination of compact  $\text{SiO}_2$  NPs is seen in Fig. 12a, b, where the ln amplitude and phase signals are shown as a function of the sample length in the cavity. Similarly, the thermal diffusivity of compact NPs for a particle size of  $216 \pm 13$  nm with a concentration of  $1 \text{ mg}\cdot\text{mL}^{-1}$  was  $1.49 \pm 0.02 \times 10^{-3} \text{ cm}^2\cdot\text{s}^{-1}$ . This is an average value from phase and amplitude of 6 measurements. On the other hand, for the porous  $\text{SiO}_2$  NPs with a size of  $207 \pm 44$  nm, the thermal diffusivity was  $1.71 \pm 0.02 \times 10^{-3} \text{ cm}^2\cdot\text{s}^{-1}$  as seen in Fig. 13a, b. The values of the thermal diffusivity of the compact and porous NPs are summarized in Table 2 with a significant increase in thermal diffusivity with respect to that of water.

**Table 2** Thermal diffusivity parameters of porous and compact SiO<sub>2</sub> nanoliquids for 1 mg·mL<sup>-1</sup> concentration measured at room temperature

Sample	Diameter	Diffusivity (10 <sup>-7</sup> m <sup>2</sup> ·s <sup>-1</sup> )	Effusivity (W·s <sup>1/2</sup> ·m <sup>-1</sup> ·K <sup>-1</sup> )	Thermal conductivity (W·m <sup>-1</sup> ·K <sup>-1</sup> )	Enrichment (%) with conductivity	References
Distilled water	–	1.44 ± 0.019	1588 ± 16	0.6026 ± 0.0007	–	1.40 × 10 <sup>-7</sup> m <sup>2</sup> ·s <sup>-1</sup> [22], 0.1588 W·s <sup>1/2</sup> ·m <sup>-1</sup> ·K <sup>-1</sup> [53], 0.607 W·m <sup>-1</sup> ·K <sup>-1</sup> [54]
Porous	207 ± 44 nm	1.71 ± 0.02	1676 ± 30	0.6914 ± 0.015	14.7%	
Compact	216 ± 13 nm	1.49 ± 0.02	1672 ± 36	0.6453 ± 0.013	7.1%	1.6 × 10 <sup>-7</sup> m <sup>2</sup> ·s <sup>-1</sup> (φ = 143 nm) [17]

φ: diameter

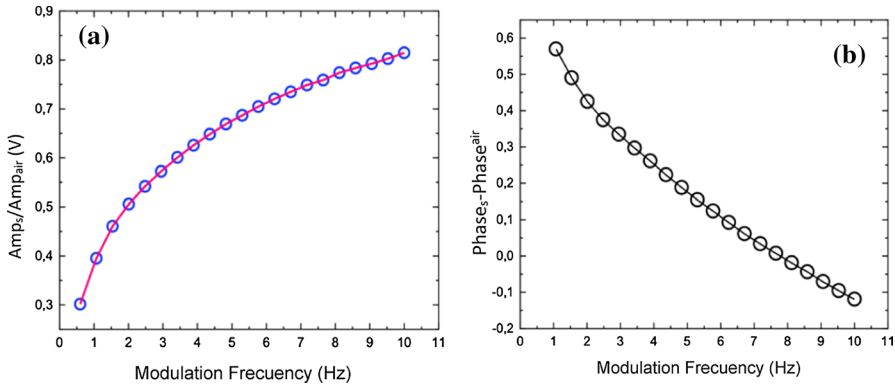


**Fig. 14** IPPE signal of normalized amplitude and phase, as a function of light modulation frequency, of compact SiO<sub>2</sub> nanoliquids of 211 nm in water base: (a) Amplitude, (b) Phase

### 3.6 Thermal Effusivity Obtained by IPPE Technique

The thermal effusivity measurements obtained by IPPE technique are shown in Fig. 14a and 14b). For the thermal effusivity of compact NPs with a particle size of  $216 \pm 13$  nm, the thermal effusivity was  $1672 \pm 36 \text{ W s}^{1/2} \cdot \text{m}^{-2} \cdot \text{K}^{-1}$ . On the other hand, for porous SiO<sub>2</sub> NPs with a size of  $207 \pm 44$  nm, the thermal effusivity was  $1676 \pm 30 \text{ W s}^{1/2} \cdot \text{m}^{-2} \cdot \text{K}^{-1}$ . The results of the normalized signal amplitude and phase are shown in Fig. 15a, b, respectively. The average values are shown in Table 2.

The relationship between the thermal diffusivity and effusivity is given by  $k = e(\alpha^{1/2})$ . The uncertainties were estimated from error propagation [43]:

$$\Delta k = k \left[ \left( \frac{\Delta e}{e} \right)^2 + \left( \frac{1}{2} \frac{\Delta \alpha}{\alpha} \right)^2 \right]^{1/2}$$

From the previous analysis, it was observed that similar particle size was obtained for compact and porous SiO<sub>2</sub> NPs ( $216 \pm 13$  nm for the compact and  $207 \pm 44$  nm for the porous SiO<sub>2</sub>). Therefore, the surface area of porous NPs was higher. From the

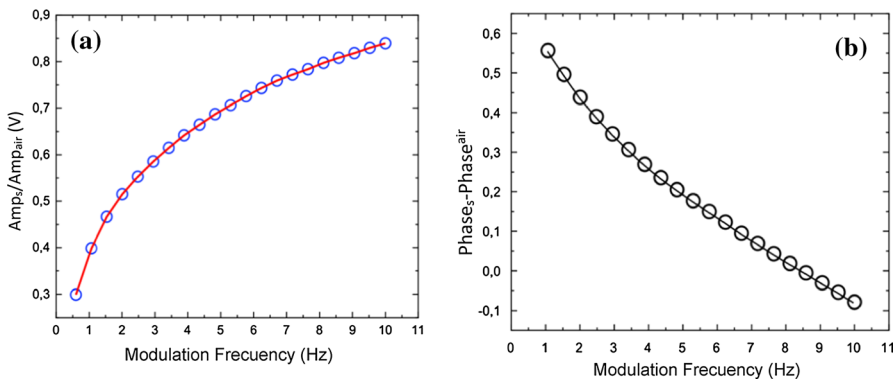


**Fig. 15** IPPE signal of normalized amplitude and phase, as a function of light modulation frequency, of the porous SiO<sub>2</sub> nanoliquids of 211 nm in water base: (a) Amplitude, (b) Phase

FTIR results, the increase in the size of the signal intensities was observed. Then, it can be concluded that there is an increase in the surface area for the porous SiO<sub>2</sub> sample, related to the surface silanol groups [32, 33]. For the compact and porous SiO<sub>2</sub> NPs, the EDS composition of the samples was mainly silicon (Si) and oxygen (O) with 67.89 wt% for O and Si of 32.11wt%, respectively. Then, the sample is 100% SiO<sub>2</sub>. From the relationship  $k = e\sqrt{D}$  of the thermal conductivity, based on the obtained values of the thermal diffusivity and effusivity, it was possible to obtain the  $k$  values of compact and porous samples. In column 5 of Table 2, the  $k$  values are summarized. The values of thermal parameters, thermal effusivity, thermal diffusivity, and thermal conductivity were similar to the values reported in the literature shown in Table 2. From the obtained results, by TWRC and IPPE techniques, an increase of 14.7% was observed in the thermal conductivity of porous SiO<sub>2</sub> NPs samples ( $0.6914 \pm 0.015 \text{ W}\cdot\text{m}^{-1}\cdot\text{K}^{-1}$ ) when compared to the thermal conductivity of the compact NPs ( $0.6453 \pm 0.013 \text{ W}\cdot\text{m}^{-1}\cdot\text{K}^{-1}$ ). From the results of the BET method [41], surface area for the porous SiO<sub>2</sub> NPs of 207 nm in size was  $1121.5 \text{ m}^2\cdot\text{g}^{-1}$  with a pore size of 2.46 nm. On the other hand, for the compact NPs with a size of 216 nm, the surface area was  $8.86 \text{ m}^2\cdot\text{g}^{-1}$ . Hence, the surface area of the porous was higher than the compact. This behavior was also reported using the techniques of the Mobil Corporation of Matter (MCM), in which highly porous solids of approximately 2 nm in diameter were prepared and surface area of  $1000 \text{ m}^2\cdot\text{g}^{-1}$  [1, 42, 44]. In the work of Chopkar, studies of the relationship between the effective thermal conductivity of nanofluids as a function of the size of the nanoparticle showed that the smaller the size, the higher the thermal conductivity of the nanofluid. This increase in conductivity was attributed to the higher surface area of the Al<sub>2</sub>Cu and Ag<sub>2</sub>Al nanoparticles [45]. On the other hand, Xie et. al., 2002 [46] support that the change in thermal conductivity is due to two factors: when the size of the nanoparticle (Al<sub>2</sub>O<sub>3</sub>) decreases, the surface area of the nanoparticle increases and therefore, its interfacial area increases. Second, the mean-free path of the phonons is estimated to be comparable to the size of the nanoparticle; then, the thermal conductivity increases when the size of the nanoparticle decreases, because the first factor is dominant. Therefore, it can be concluded that more complete models are still lacking to explain the experiments as a function of nanoparticle size, shape, volume fraction, surface area, and host fluid mixing, and these have not been developed yet.

On the other hand, a theoretical hydrodynamic model of the effective thermal conductivity of Si nanoporous media for rigid particles in a fluid ( $k = k_{pSiO_2}^{eff}$ ), adapted for porous SiO<sub>2</sub> and to support the results that were used [47–49]:

$$k_{pSiO_2}^{eff} = k_m \frac{2k_m + (1 + 2\alpha)k_p + 2\varepsilon[(1 - \alpha)k_p - k_m]}{2k_m + (1 + 2\alpha)k_p - \varepsilon[(1 - \alpha)k_p - k_m]}, \quad (3)$$

where  $\varepsilon$  is the porosity,  $k_p$  is the nanopore thermal conductivity,  $k_m$  is the bulk thermal conductivity of the host medium being the bulk SiO<sub>2</sub> and  $\alpha$  which is a dimensionless parameter that describes the interaction between the nanopore and the medium, given by [48]:  $\alpha = Rk_m/r_p$  where  $r_p$  is the nanopore radius and  $R$  is the



thermal boundary resistance coefficient given by [50]:  $R = \frac{4}{C_m v_m} + \frac{4}{C_p v_p}$  where  $C_m, v_m, C_p$  y  $v_p$  represents the specific heat capacities and phonons group velocities of the bulk medium and the mesoporous, respectively. From the Knudsen expression, in the asymptotic limit is [51]  $k_p$  is

$$k_p = \frac{3k_p^0}{Kn^2} \left[ \frac{3\pi Kn}{\arctan(2\pi Kn)} - 1 \right], \quad \text{where } Kn = \frac{\Lambda_{p, SiO_2}}{r_p} \quad (4)$$

where  $k_p^0$  is the value of thermal conductivity for air,  $Kn$  is the Knudsen number and  $\Lambda_{p, SiO_2}$  is the mean-free path. Using the experimental values obtained:  $\epsilon = 0.40$ ,  $k_p = 7.95 \times 10^{-5} \frac{W}{mK}$ ,  $k_m = 1.3 \frac{W}{mK}$ ,  $r_p = 2.46 nm$ ,  $R = 9.91 \times 10^{-6} m^2 \cdot K \cdot J^{-1}$ ,  $\alpha = 4773.57$ ,  $k_p^0 = 0.026 \frac{W}{mK}$ ,  $\Lambda_{p, SiO_2} = 256 nm$  and  $C_m = 4.18 \times 10^{-6} J \cdot m^{-3} \cdot K^{-1}$ ,  $C_p = 256 J \cdot m^{-3}$ ,  $v_m = 294248.825$ ,  $v_{SiO_2} = 1804 m \cdot s^{-1}$ . For constant viscosity at  $T = 300 K$ . Using these values, the conductivity obtained for the porosity and pore size with the model was  $k_{pSiO_2}^{eff} = 0.6500 \frac{W}{mK}$  which is a value very close to the experimental value obtained  $0.6914 W \cdot m^{-1} \cdot K^{-1}$  (Table 2).

In the same way, the thermal conductivity for the compact  $SiO_2$  NPs was calculated using the Hamilton-Crosser model [52]:

$$k_{eff} = k_L \left( \frac{k_m + (n-1)k_L - (n-1)\phi_m(k_L - k_m)}{k_m + (n-1)k_L + \phi_m(k_L - k_m)} \right) \quad (5)$$

where  $k_L = 0.6026 W \cdot m^{-1} \cdot K^{-1}$  is the thermal conductivity of base fluid,  $n = \frac{1}{3}$  is the sphericity factor and  $\phi_m = 0.039$  is the volume percent of the NPs in the base fluid. The value of the thermal conductivity obtained from the model was  $0.6102 W \cdot m^{-1} \cdot K^{-1}$  similar to the experimental value which was  $0.6453 W \cdot m^{-1} \cdot K^{-1}$  as seen in Table 2. Therefore, the thermal conductivity for the hydrodynamic model depends on two parameters: porosity and particle pore size. Then, for pore sizes less than 2.46 nm, the thermal conductivity was  $0.65 W \cdot m^{-1} \cdot K^{-1}$ , increasing with respect to the compact nanoparticle.

Table 2 summarizes the experimental values obtained. It can also be seen that the values are similar to the base liquid reported in the literature [1].

## 4 Conclusions

The compact monodisperse  $SiO_2$  NPs were synthesized using the Stöber method. Due to the modification of the reagents, the synthesis was done in a shorter time than that reported in previous articles without compromising its structure. By adding a cationic surfactant to the synthesis using the modified Stöber method, monodisperse porous  $SiO_2$  NPs were synthesized with a shorter time than the compact ones. The pH value was fundamental to control the size of the nanostructure as well as the synthesis time and the dropping of the silicon precursor, with a constant speed. The FTIR and EDS analysis showed the typical functional groups and elemental composition associated to the  $SiO_2$  NPs. The compact and porous  $SiO_2$  NPs were

analyzed using the TWRC and IPPE techniques which were used for the first time to determine the porous SiO<sub>2</sub> NPs thermal diffusivity, effusivity, and conductivity. An increase of thermal conductivity of the porous SiO<sub>2</sub> NPs was observed compared to the compact nanoparticles, with an enrichment of the 14.7%. On the other hand, a hydrodynamic model and the Hamilton-Crosser model were adapted to calculate the thermal conductivity of the porous and compact SiO<sub>2</sub> NPs, respectively to support the effect of the presence of porosity and pore size on thermal conductivity. The results of our experimental analysis showed close similarity with the theoretical values with pore radius of 2.46 nm, where the influence of the pore and pore size of the nanoparticle is relevant. The TWRC and IPPE techniques are promising techniques to analyze transparent, opaque, and thermally thick nanofluids.

**Acknowledgements** We would like to thank CONACYT, COFAA-IPN, EDI for their support. Dr Eduardo San Martin from CICATA-Legaria for the technical assistance and to Eng. Marcela Guerrero from CINVESTAV for FTIR measurements.

**Author Contributions** GV: methodology, investigation, data curation. JP: conceptualization, supervision, methodology, investigation, writing—original draft. LG: methodology. GF: methodology. SR: methodology. CP: methodology, writing—review and editing. RI: methodology, Writing—review & editing. CO: methodology, writing—review and editing.

**Funding** No funding was received for this research.

## Declarations

**Conflict of interest** The authors declare that they have no known competing financial interests for the work reported in this paper.

## References

1. J. Jisha, T. Lincy, K. Achamma, V.P.N. Nampoory, G. Sajan, *Micropor. Mesopor. Mat.* **244**, 171–179 (2017)
2. K.B. Seljak, P. Kocbek, M. Gašperlin, J. Drug Deliv. Sci. Technol. **59**, 101906 (2020)
3. B. Yang, Y. Chen, J. Shi, *Mat. Sci. Eng. R* **137**, 66 (2019)
4. X. Di, L. Shen, J. Jiang, M. He, Y. Cheng, L. Zhou, X. Liang, W. Xiang, *J. Alloy Compd.* **729**, 526 (2017)
5. A. Mehmood, H. Ghafar, S. Yaqoob, U.F. Gohar, B. Ahmad, *J. Develop. Drugs* **6**, 1 (2017)
6. Y. Yan, S.C. King, M. Li, T. Galy, M. Marszewski, J.S. Kang, L. Pilon, Y. Hu, S.H. Tolbert, *J. Phys. Chem. C* **123**(35), 21721 (2019)
7. B. Sun, X. Zhen, X. Jiang, *Biomater. Sci.* **9**, 3603 (2021)
8. M. Manzano, M. Vallet-Regí, *Adv. Funct. Mater.* **30**, 1902634 (2020)
9. H. He, S. Meng, H. Li, Q. Yang, Z. Xu, X. Chen, Z. Sun, B. Jiang, C. Li, *Microchim. Acta* **188**, 154 (2021)
10. S. Jafari, H. Derakhshankhah, L. Alaei, A. Fattahi, B.S. Varnamkhasti, A.A. Saboury, *Biomed. Pharmacother.* **109**, 1100 (2019)
11. M. Komiyama, K. Ariga, *Mol. Catal.* **475**, 110492 (2019)
12. T.T.H. Thi, V.D. Cao, T.N.Q. Nguyen, D.T. Hoang, V.C. Ngo, D.H. Nguyen, *Mat. Sci. Eng. C* **99**, 631 (2019)
13. A. Watermann, J. Brieger, *Nanomaterials* **7**(7), 189 (2017)
14. N.S. Zaharudin, E.D.M. Isa, H. Ahmad, M.B.A. Rahman, K. Jumbri, *J. Saudi Chem. Soc.* **24**(3), 289 (2020)
15. V. Niculescu, *Front. Mater.* **7**(36), 1 (2020)

16. A. Netzahual, J. F. Sánchez Ramírez, J. L. Jiménez Pérez, Appl. Phys. A **126**, 172 (2020)
17. A. Netzahual-Lopantzi, J.F. Sánchez-Ramírez, J.L. Jiménez-Pérez, D. Cornejo-Monroy, G. López-Gamboa, Z.N. Correa-Pacheco, Appl. Phys. A **125**, 588 (2019)
18. J.L. Jiménez-Pérez, G. López-Gamboa, J.F. Sánchez-Ramírez, Z.N. Correa-Pacheco, A. Netzahual-Lopantzi, A. Cruz-Orea, Int. J. Thermophys. **42**, 107 (2021)
19. Y. Ma, Y. Hong, S. Qiao, Z. Lang, X. Liu, Opt. Lett. **47**, 601 (2022)
20. L. Osoltseva, M. Korobov, M. Proskurnin, J. Appl. Phys. **128**, 190901 (2020)
21. J.A. Balderas-López, A. Mandelis, J.A. Garcia, Rev. Sci. Instrum. **71**, 2933 (2000)
22. P.R.B. Pedreira, L. Hirsch, J.R.D. Pereira, A.N. Medina, A.C. Bento, M.L. Baesso, Rev. Sci. Instrum. **74**(1), 808 (2003)
23. W. Stöber, A. Fink, E. Bohn, J. Colloid Interface Sci. **26**(1), 62 (1968)
24. H. Liu, H. Li, Z. Ding, A. Fu, H. Wang, P. Guo, J. Yu, C. Wang, X. Zhao, J. Clust. Sci. **23**, 273 (2012)
25. L. Luo, Y. Liang, E.S. Erichsen, R. Anwander, J. Colloid Interface Sci. **495**, 84 (2017)
26. M. Grün, K. Unger, A. Matsumoto, K. Tsutsumi, Micropor. Mesopor. Mat. **27**(2–3), 207 (1999)
27. G. Lara-Hernández, E. Suaste-Gómez, A. Cruz-Orea, J. G. Mendoza-Alvarez, F. Sánchez-Sinencio, J. P. Varcárcel, A. García-Quiroz, Int. J. Thermophys. **34**, 962 (2013)
28. J. Caerels, C. Glorieux, J. Thoen, Rev. Sci. Instrum. **69**, 2452 (1998)
29. J.A. Balderas-López, A. Mandelis, Int. J. Thermophys. **23**, 605 (2002)
30. J. Balderas-López, M. Jaime-Fonseca, J. Diaz-Reyes, Y. Gómez-Gómez, M. Bautista-Ramírez, A. Diosdado, G. Gálvez-Coyt, Braz. J. Phys. **46**, 105 (2015)
31. A. Hernández, M.L. Barrios, M.L. Sánchez, Mater. Today Proc. **13**(2), 446 (2019)
32. M.S. El-Shall, S. Li, T. Turkki, D. Graiver, U. Pernisz, M. Baraton, J. Phys. Chem. **99**, 17805 (1995)
33. S. M. Holmes, V. L. Zholobenko, A. Thursfield, R. J. Plaisted, C. S. Cundy, J. Dwyer, J. Chem. Soc., Faraday Trans. **94**, 2025 (1998)
34. V.L. Zholobenko, S.M. Holmes, C.S. Cundy, J. Dwyer, Microporous Mater. **11**(1–2), 83 (1997)
35. Y. Chen, X. Shi, B. Han, H. Qin, Z. Li, Y. Lu, J. Wang, Y. Kong, J. Nanosci. Nanotechnol. **12**(9), 7239 (2012)
36. S. Jana, A. Mochizuki, S. Namba, Catal. Surv. Asia **8**, 1 (2004)
37. Q. Cai, Z. Luo, W. Pang, Y. Fan, X. Chen, F. Cui, Chem. Mater. **13**(2), 258 (2001)
38. N.N.A. Ghani, M.A. Saeed, M.H. Hashim, Mal. J. Fund. Appl. Sci. **13**(3), 178 (2017)
39. B.M. Vinoda, M. Vinuth, Y.D. Bodke, J. Manjanna, J. Environ. Anal. Toxicol. **5**(6), 336 (2015)
40. S. Lowell, J.E. Shields, *Powder Surface Area and Porosity* (Springer, Dordrecht, 1991)
41. M.T.K.A. Cychosz, R. Guillet-Nicolas, J. García-Martínez, Chem. Soc. Rev. **46**, 389 (2016)
42. T. Linssen, K. Cassiers, P. Cool, E.F. Vansant, Adv. Colloid Interfac. **103**(2), 121 (2003)
43. M. Drogg, *Dealing with Uncertainties, a Guide to Error Analysis* (Springer, Berlin, 2007)
44. J. Lu, J. Wang, K.T. Hassan, A. Talmantaite, Z. Xiao, M.R.C. Hunt, L. Šiller, Sci. Rep. **10**, 11743 (2020)
45. M. Chopkar, Metall. Mater. Trans. A. **39A**, 1535 (2008)
46. H. Xie, J. Wang, T. Xi, Y. Liu, F. Ai, J. Appl. Phys. **91**(7), 4568 (2002)
47. H. Machrafi, G. Lebon, Phys. Lett. A **379**, 968 (2015)
48. J.C. Maxwell, *Treatise on Electricity and Magnetism*, 2nd edn. (Clarendon, Oxford, 1881)
49. D. Bruggeman, Ann. Phys. **24**, 636 (1935)
50. A. Minnich, G. Chen, Appl. Phys. Lett. **91**, 073105 (2007)
51. S. Hess, Z. Naturforsch. **32a**, 678 (1977)
52. R.L. Hamilton, O.K. Crosser, I & EC Fundam. **1**, 187 (1962)
53. G.A. López-Muñoz, J.A. Balderas-López, Thermochim. Acta **579**, 40 (2014)
54. M.L. Huber, R.A. Perkins, D.G. Friend, J.V. Sengers, M.J. Assael, I.N. Metaxa, K. Miyagawa, R. Hellmann, E. Vogel, J. Phys. Chem. Ref. Data **41**(3), 033102 (2012)

**Publisher's Note** Springer Nature remains neutral with regard to jurisdictional claims in published maps and institutional affiliations.

Springer Nature or its licensor (e.g. a society or other partner) holds exclusive rights to this article under a publishing agreement with the author(s) or other rightsholder(s); author self-archiving of the accepted manuscript version of this article is solely governed by the terms of such publishing agreement and applicable law.

## Authors and Affiliations

**U. O. García-Vidal<sup>1</sup> · J. L. Jiménez-Pérez<sup>1</sup> · G. López-Gamboa<sup>2</sup> ·  
R. Gutiérrez-Fuentes<sup>3</sup> · J. F. Sánchez-Ramírez<sup>4</sup> · Z. N. Correa-Pacheco<sup>5</sup> ·  
I. C. Romero-Ibarra<sup>1</sup> · A. Cruz-Orea<sup>6</sup>**

- <sup>1</sup> Unidad Profesional Interdisciplinaria en Ingeniería y Tecnologías Avanzadas, Instituto Politécnico Nacional, Avenida Instituto Politécnico Nacional No. 2580, Col Barrio La Laguna Ticomán, Gustavo A. Madero, C.P. 07340 Mexico City, Mexico
- <sup>2</sup> Instituto Tecnológico de Toluca, Avenida Tecnológico S/N. Colonia Agrícola, Bellavista, La Virgen, C.P. 52149 Metepec, Mexico State, Mexico
- <sup>3</sup> Tecnológico de Estudios Superiores de Villa Guerrero, división de Ingeniería Electrónica, Carretera Federal Toluca - Ixtapan de La Sal. Km. 64.5, Col. La Finca, Villa Guerrero, Mexico State, Mexico
- <sup>4</sup> Centro de Investigación en Biotecnología Aplicada, Instituto Politécnico Nacional, ExHacienda de San Juan Molino. Km 1.5 de la Carretera Estatal Santa Inés Tecuexcomac-Tepetitla. Tepetitla, C. P. 90700 Tlaxcala, Mexico
- <sup>5</sup> Centro de Desarrollo de Productos Bióticos, Instituto Politécnico Nacional, Carretera Yautepec-Jojutla, Km. 6, Calle CEPROBI No. 8, Col. San Isidro, C.P. 62731 Yautepec, Morelos, Mexico
- <sup>6</sup> Departamento de Física, CINVESTAV-IPN, Av. Instituto Politécnico Nacional, No. 2508, Col. San Pedro Zacatenco, C.P. 07360 Mexico City, Mexico